ARTICLE   **Open Access**

Dimensional control of interface coupling-induced ferromagnetism in CaRuO₃/SrCuO₂ superlattices

Li Zhe[1,2], Shi Wenxiao[1,2], Zhang Jine[3], Zheng Jie[1,2], Wang Mengqin[1,2], Zhu ZhaoZhao[1,2], Han Furong[3], Zhang Hui[3], Xie Liming[4], Yunzhong Chen [1], Fengxia Hu [1,2], Baogen Shen [1,2,5], Yuansha Chen [1,2] and Jirong Sun[1,2,6]

Abstract
Due to the strong interactions from multiple degrees of freedom at the interfaces, electron-correlated oxide heterostructures have provided a promising platform for creating exotic quantum states. Understanding and controlling the coupling effects at the oxide interface are prerequisites for designing emergent interfacial phases with desired functionalities. Here, we report the dimensional control of the interface coupling-induced ferromagnetic (FM) phase in perovskite-CaRuO₃/infinite-layered-SrCuO₂ superlattices. Structural analysis reveals the occurrence of chain-type to planar-type structural transitions for the SrCuO₂ layer as the layer thickness increases. The Hall and magnetoresistance measurements indicate the appearance of an interfacial FM state in the originally paramagnetic CaRuO₃ layers when the CaRuO₃ layer is in proximity to the chain-type SrCuO₂ layers; this superlattice has the highest Curie temperature of ~75 K and perpendicular magnetic anisotropy. Along with the thickness-driven structural transition of the SrCuO₂ layers, the interfacial FM order gradually deteriorates and finally disappears. As shown by the X-ray absorption results, the charge transfer at the CaRuO₃/chain-SrCuO₂ and CaRuO₃/plane-SrCuO₂ interfaces are different, resulting in dimensional control of the interfacial magnetic state. The results from our study can be used to facilitate a new method to manipulate interface coupling and create emergent interfacial phases in oxide heterostructures.

Introduction

ABO₃-type perovskite transition-metal oxides (TMOs) exhibit a wide variety of fascinating properties due to their highly correlated d-band electrons; these properties include high-T_C superconductivity, colossal magnetoresistance, ferroelectricity, and multiferroicity[1–6]. Benefiting from advances in fabrication techniques, the precise control of layer-by-layer growth of different oxides in the form of heterostructures or superlattices (SLs) has become possible[7–10]. Due to the strong interplay of multiple degrees of freedom at the interface, the physical properties of the oxide layer could be significantly different from those of the bulk phase, providing a rich

source of emergent quantum phases with attractive functionalities[11–13]. Thus, intensive research has been devoted to artificial oxide heterostructures, exploring the effect of interface coupling[14,15]. Interfacial ferromagnetic (FM) phases generated from two non-FM materials are of special importance in both fundamental physics and potential applications in spintronics[16,17].

In this study, we focus on a special SL structure formed by the perovskite ruthenate CaRuO₃ (CRO) and the infinite-layered cuprate SrCuO₂ (SCO). CRO with an orthorhombic structure is a paramagnetic (PM) metal that shows unique non-Fermi liquid behavior at low temperatures[18,19]. Compared with its sister system, the itinerant ferromagnet SrRuO₃ (SRO), CRO has a stronger orthorhombic distortion, which causes degeneracy of the t_{2g} band and a relatively lower near-Fermi-surface density of states $N(E_F)$[19–21]. Thus, CRO maintains the PM behavior down to at least 2 K in both bulk and thin film forms[18,22]. On the other hand, bulk SCO is an

Correspondence: Yuansha Chen (yschen@iphy.ac.cn) or
Jirong Sun (jrsun@iphy.ac.cn)
¹Beijing National Laboratory for Condensed Matter Physics and Institute of Physics, Chinese Academy of Sciences, Beijing 100190, China
²School of Physical Sciences, University of Chinese Academy of Sciences, Beijing 100049, China
Full list of author information is available at the end of the article

antiferromagnetic (AFM) insulator, with a layered structure that can be regarded as a perovskite-like framework with missing apical oxygen ions[23,24]. When SCO is grown as a film, a thick film usually shows planar (P)-type oxygen coordination, where positively charged Sr^{2+} and negatively charged CuO^{2-} planes are alternately stacked along the normal direction of the film[25,26]. Upon reducing the film thickness, the P-type structure of the SCO layer transforms to a chain (C)-type structure with the CuO_2^{2-} planes perpendicular to the film plane to avoid electrostatic polar instability[24]. Dimensional control of the lattice structure of the SCO layers and oxygen coordination have been achieved in both SCO bare films and SCO-involved heterostructures[27,28]. Thus, when SCO is grouped with CRO, the mismatch of apical oxygen and the large polarity discontinuity may cause additional effects associated with interfacial reconstruction, leading to unusual properties that cannot be obtained in bare films or ordinary perovskite/perovskite heterostructures[27,29].

Here, highly epitaxial CRO/SCO SLs with a fixed CRO sublayer thickness and varied SCO sublayer thickness were prepared on $(LaAlO_3)_{0.3}$-$(Sr_2AlTaO_6)_{0.7}$ (LSAT) and $SrTiO_3$ (STO) substrates. Structural analysis revealed a C-type to P-type structural transition of the SCO layer when the layer thickness increased from 1 unit cell (u.c.) to 4 u.c. in each SL period. Hall and magnetoresistance (MR) measurements indicated the appearance of the FM phase at the CRO/C-SCO interface. The maximal Curie temperature of ~75 K occurred in the SL with full C-type SCO sublayers, accompanied by the appearance of perpendicular magnetic anisotropy (PMA). By dimensionally controlling the oxygen coordination at the CRO/SCO interface, the interfacial FM order could be significantly tuned and finally disappeared at the CRO/P-SCO interface. X-ray absorption (XAS) measurements revealed significant Ru-to-Cu charge transfer at the CRO/C-SCO interface, resulting in a much greater hole density in the CRO sublayers and, thus, FM ordering. Moreover, the hybridization between Ru and Cu $d_{3z^2-r^2}$ orbitals in a lower bonding band caused preferential $d_{3z^2-r^2}$ occupancy of Ru ions, which was responsible for the PMA of CRO/C-SCO SLs. Our results provide a feasible way to manipulate interface coupling and thus form promising interfacial phases in perovskite/infinite-layered oxide heterostructures.
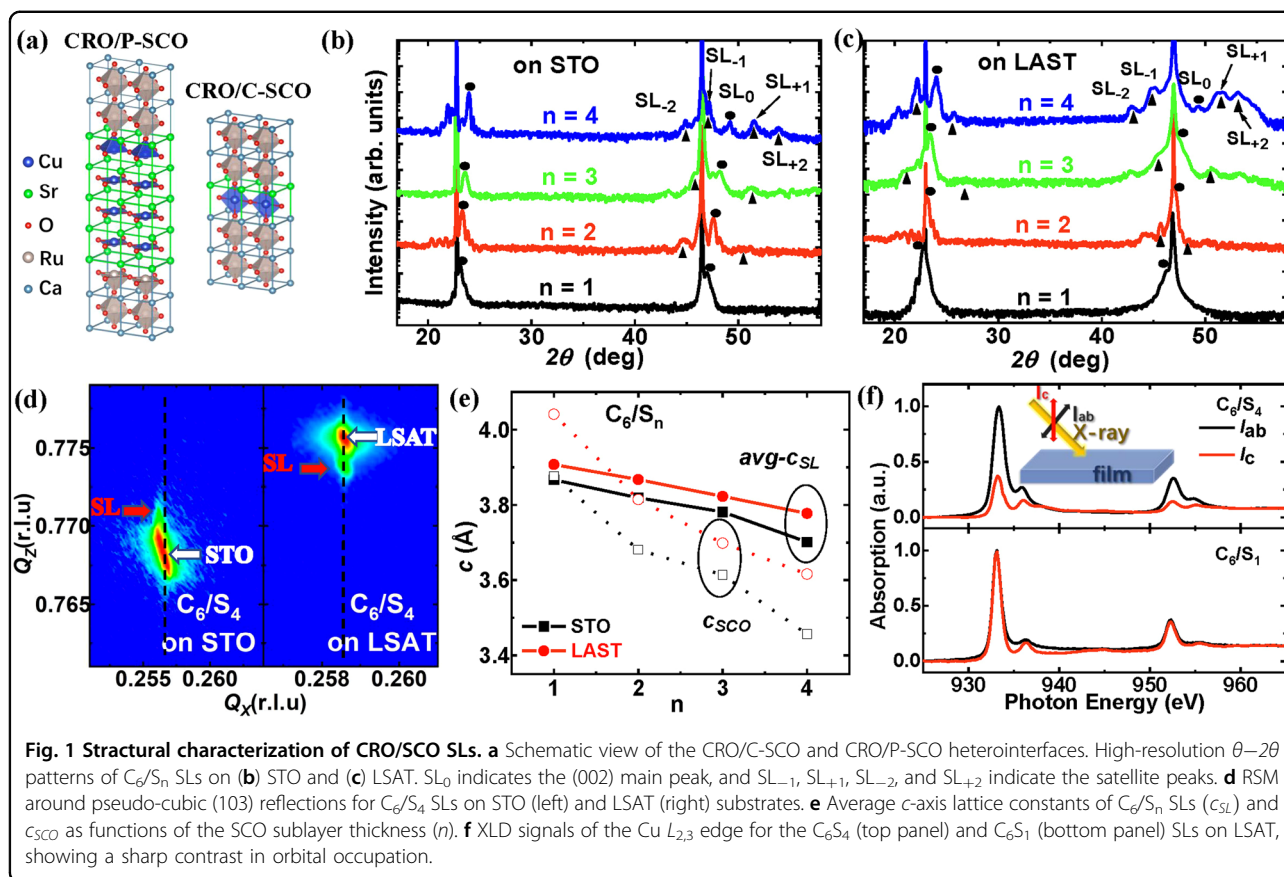
Results and discussion
Dimensional control of the lattice structure of SCO sublayers in CRO_6/SCO_n superlattices

$[(CRO)_6/(SCO)_n]_8$ (C_6/S_n) SLs, with a CRO sublayer of 6 u.c. and an SCO sublayer of n u.c. in each period, were epitaxially grown on (001)-oriented LSAT and STO substrates by pulsed laser deposition. The deposition parameters were optimized to achieve high-quality and flat SLs

(see Fig. S1 in the Supplementary Materials). As mentioned above, the SCO layers transferred from the P-type to C-type structure as the layer thickness decreased (the critical thickness was 2 ~ 3 u.c. depending on the substrate strain)[25]. This caused two types of interfaces in the CRO/SCO heterostructures, i.e., the CRO/P-SCO and the CRO/C-SCO interfaces, as shown in Fig. 1a. To determine the effect of the dimensionality of the SCO layer on interface coupling, four C_6/S_n SLs with n ranging from 1 to 4 were prepared. The corresponding X-ray diffraction (XRD) patterns of the SLs on the LSAT and STO substrates are shown in Fig. 1b, c, respectively. The (001) main peaks, along with a series of satellite peaks, were clearly observed; these were the typical features of the XRD spectra of the SL structure. With increasing SCO sublayer thickness, the SL_0 main peak showed systematic variation, shifting from 46.44° (or 46.96°) for the C_6/S_1 SL to 48.14° (or 49.19°) for the C_6/S_4 SL on the LSAT (or STO) substrate. The average out-of-plane lattice constants of the SLs (c_{SL}) deduced from the SL_0 peaks are summarized in Fig. 1e. The SL_0 peak significantly decreased with increasing SCO thickness, from 3.91 Å (or 3.87 Å) to 3.78 Å (or 3.70 Å) for the SLs on LSAT (or STO). These results strongly indicated the structural transition of the SCO sublayers because P-SCO had a much smaller c-axis lattice constant (~3.45 Å) than C-SCO (~3.80 Å). Generally, the average c_{SL} of C_6/S_n SLs could be effectively expressed using the formula $c_{SL} = (6 \times c_{CRO} + n \times c_{SCO})/(n + 6)$, where c_{CRO} and c_{SCO} represent the lattice parameters of the CRO and SCO sublayers, respectively. Further analysis of the reciprocal space mapping indicated that the SLs were fully in-plane strained, similar to what was observed in the bare CRO films with equivalent thicknesses. For example, the diffraction spot of the C_6/S_4 SL (marked by the red arrow in Fig. 1d) is located just below (or above) that of the LSAT (or STO) substrate; thus, both SLs were coherently strained to the substrate without lattice relaxation. This deduction was also applicable to other samples. Therefore, we considered that the CRO sublayers in the SLs had the same c_{CRO} as that of the bare film. Thus, according to the above formula, c_{SCO} for different SLs could be directly deduced. The c_{SCO} values were ~3.88 Å for the SCO sublayers in the C_6/S_1 SL and ~3.46 Å for the SCO layers in the C_6/S_4 SL (dashed lines in Fig. 1e); these results were consistent with the reported values of C-SCO and P-SCO, respectively. Thus, the interface coupling was likely determined by the CRO/C-SCO connections for the C_6/S_1 SL and by the CRO/P-SCO connections for the C_6/S_4 SL. In contrast, the SCO sublayers in the C_6/S_2 and C_6/S_3 SLs were C-SCO and P-SCO mixed phases, respectively, presenting intermediate c_{SCO} values.

Further evidence for the thickness-driven structural transition of SCO was obtained by X-ray linear dichroism (XLD) measurements acquired in total electron yield (TEY) mode. The orbital occupancies of the Cu $d_{x^2-y^2}$ and $d_{3z^2-r^2}$ orbitals were probed by the XAS spectra obtained
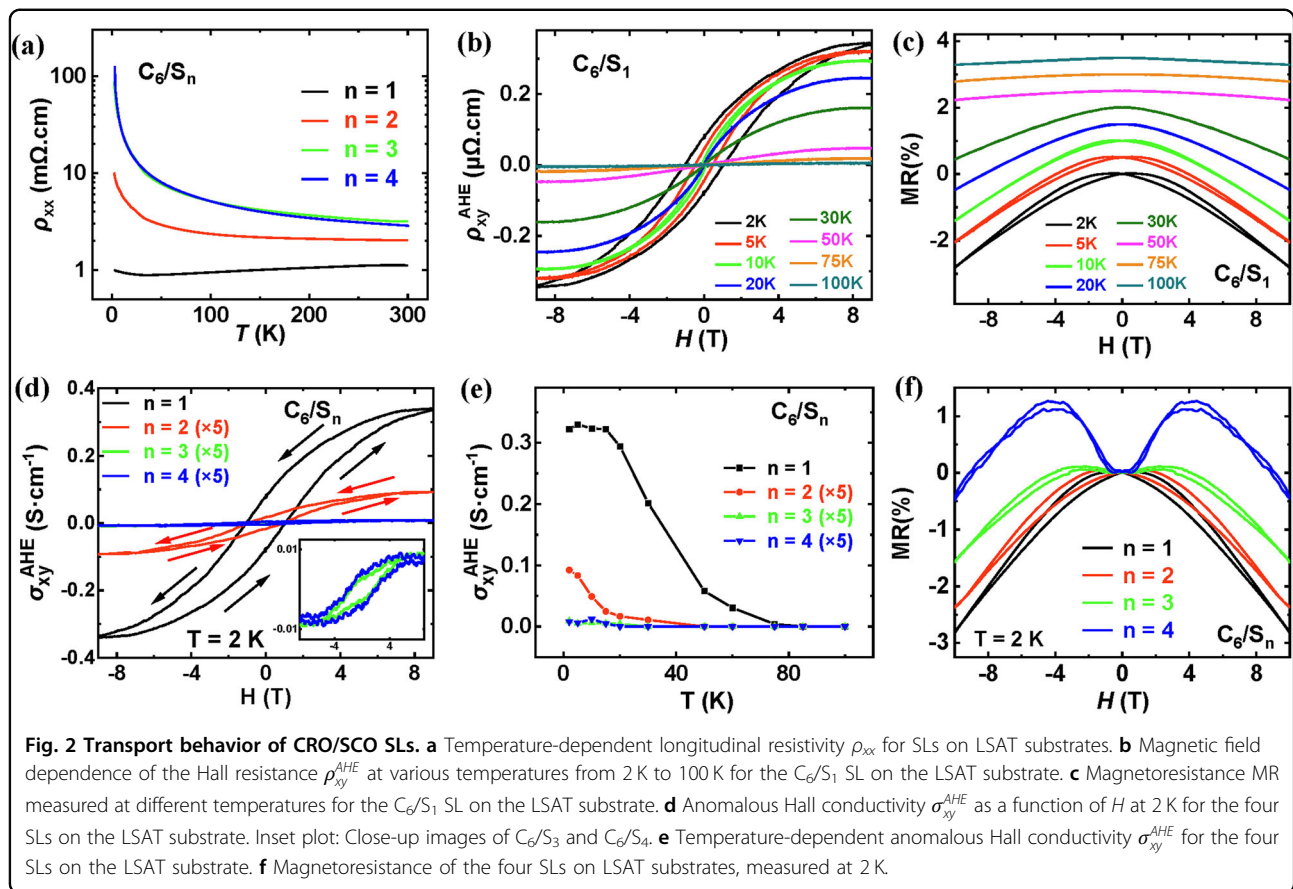
Fig. 1 Stractural characterization of CRO/SCO SLs. a Schematic view of the CRO/C-SCO and CRO/P-SCO heterointerfaces. High-resolution $\theta-2\theta$ patterns of C_6/S_n SLs on **(b)** STO and **(c)** LAST. SL_0 indicates the (002) main peak, and SL_{-1}, SL_{+1}, SL_{-2}, and SL_{+2} indicate the satellite peaks. **d** RSM around pseudo-cubic (103) reflections for C_6/S_4 SLs on STO (left) and LSAT (right) substrates. **e** Average c-axis lattice constants of C_6/S_n SLs (c_{SL}) and c_{SCO} as functions of the SCO sublayer thickness (n). **f** XLD signals of the Cu $L_{2,3}$ edge for the C_6S_4 (top panel) and C_6S_1 (bottom panel) SLs on LSAT, showing a sharp contrast in orbital occupation.

with in-plane (I_{ab}) and out-of-plane (I_c) polarized X-rays, respectively. Figure 1f shows the corresponding XAS and XLD signals for the C_6S_4 and C_6S_1 SLs on LSAT. Evidently, for the C_6S_4 SL, the absorption for photon polarization parallel to the CuO_2 sheets (I_{ab}) greatly exceeded that for polarization along the c axis, i.e., $I_{ab} > I_c$. This result was consistent with the orbital configuration of thick SCO films with P-type structures[25,28,29] since the holes in P-SCO predominantly occupied the planar Cu d_{x2-y2} orbital, which strongly hybridized with the O 2p orbitals in CuO_2 layers. However, the C-type SCO results differed due to the presence of apical oxygen. In this case, the holes were equally distributed in the d_{x2-y2} and d_{3z2-r2} orbitals; thus, the peak intensities of I_{ab} and I_c were nearly identical. This was the case that we observed in the C_6S_1 SL. All these features confirmed the high quality of the C_6S_n SLs, with the dimensionally controllable structure of the SCO sublayers.

Emergent interfacial ferromagnetism in CRO_6/SCO_n superlattices

The XRD and XLD analyses indicate the occurrence of structural transitions for the SCO layer in the SLs as the SCO layer thickness increases. In general, interface coupling is affected by this phase transition, which results in changes in the matching/mismatching of apical oxygen ions at interfaces and polarity discontinuities across interfaces. We are interested in determining what happens to the CRO layer, which is in close proximity to the SCO. The electronic transport properties of the SLs were measured using the standard four-probe configuration. Figure 2a shows the longitudinal resistivity ρ_{xx} as a function of temperature (ρ_{xx}-T) for the C_6/S_n ($n=1$–4) SLs on LSAT. C_6/S_1 SL has the lowest ρ_{xx} and shows essentially metallic behavior. With increasing n, ρ_{xx} gradually increases and becomes completely semiconducting when $n=3$ and 4. Since SCO is highly insulating, the electronic transport process of SLs should be solely dominated by the CRO sublayers[30]. Thus, based on the different ρ_{xx}-T dependences and compared with the CRO/P-SCO interface, the CRO/C-SCO interface supports metallic transport. As shown later, the CRO/C-SCO interface results in a higher carrier density for the CRO sublayers than the CRO/P-SCO interface.
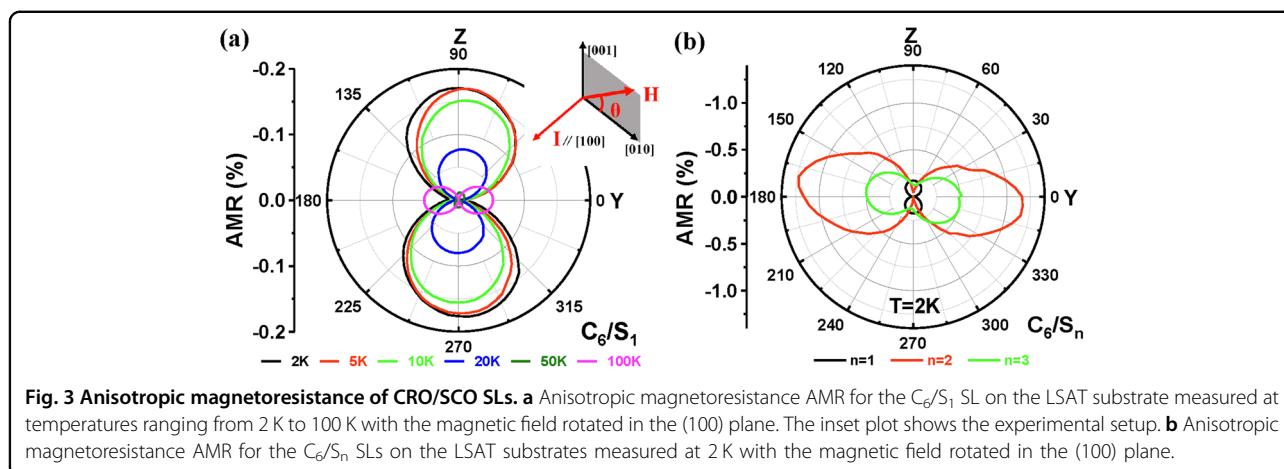
To explore the emergent phenomenon at the CRO/SCO interface, we further investigated the Hall transport properties of the SLs using the Hall-Bar configuration. Generally, for a ferromagnet, the Hall resistivity can be described by $\rho_{xy} = R_H \cdot H + R_s \cdot M$, where the first term represents the ordinary Hall effect and is proportional to the applied

Fig. 2 Transport behavior of CRO/SCO SLs. a Temperature-dependent longitudinal resistivity ρ_{xx} for SLs on LSAT substrates. **b** Magnetic field dependence of the Hall resistance ρ_{xy}^{AHE} at various temperatures from 2 K to 100 K for the C_6/S_1 SL on the LSAT substrate. **c** Magnetoresistance MR measured at different temperatures for the C_6/S_1 SL on the LSAT substrate. **d** Anomalous Hall conductivity σ_{xy}^{AHE} as a function of H at 2 K for the four SLs on the LSAT substrate. Inset plot: Close-up images of C_6/S_3 and C_6/S_4. **e** Temperature-dependent anomalous Hall conductivity σ_{xy}^{AHE} for the four SLs on the LSAT substrate. **f** Magnetoresistance of the four SLs on LSAT substrates, measured at 2 K.

magnetic field H, and the second term represents the anomalous Hall resistivity (ρ_{xy}^{AHE}) and proportional to spontaneous magnetization M. Figure 2b shows the ρ_{xy}^{AHE}-H curves for the C_6/S_1 SL on the LSAT substrate collected at temperatures ranging from 2 K to 100 K. The raw Hall curves for the four SLs can be found in Supplementary Fig. S2. Notably, the hysteresis loops are clearly observed in the ρ_{xy}^{AHE}-H curves measured below 20 K. This hysteresis behavior can be effectively fitted by a modified Heaviside step function expressed as $\rho_{xy}^{AHE} = 4\pi R_s \cdot M = 4\pi R_s \cdot M_s \cdot \tanh(h \cdot (H \pm H_c))$, where R_s, M_s, H_c and h are the AHE coefficient, the saturation magnetization, the coercive field and the slope of the ρ_{xy}^{AHE}-H curve at H_c, respectively (see Fig. S3 in the Supplement). This result provides solid evidence for the formation of long-range FM order. The ρ_{xy}^{AHE}-H curve measured at 2 K has the highest saturation ρ_{xy}^{AHE} of 0.34 µΩ.cm and the largest H_C of ~1 T. The hysteresis loop only closes at the highest field of the present experiment, indicating a saturation field higher than 9 T for the C_6/S_1 SL. This finding is similar to the large saturation field observed in the SrIrO$_3$-based heterostructures, where the freezing of phonons at low temperatures was considered to be the reason for high saturation fields[31]. As the temperature increases, the H_C quickly decreases, and the hysteresis loop disappears when the temperature exceeds 30 K.

However, the AHE signals remain visible up to 75 K. As mentioned above, the transport measurements mainly reflect the properties of the CRO sublayers. Thus, the remarkable observation of the AHE signal strongly indicated the appearance of the FM phase in the original PM CRO sublayers. A similar trend is also identified from the MR-H curves. Figure 2c shows the magnetic field dependence of MR $= (R_H-R_0)/R_0$ obtained at 2 K to 100 K, where R_H and R_0 are the longitudinal resistances measured with and without an out-of-plane field, respectively. Butterfly shaped loops with two broad peaks at $\pm H_C$ are clearly observed in the MR-H curves at low temperatures; these correspond to the reconstitution of magnetic domains in the SL. The MR at 9 T gradually decreases with increasing temperature, from 2.8% at 2 K to 0.2% at 75 K.

Hall measurements were also performed for other C_6/S_n SLs, and hysteresis behavior was generally observed at low temperatures (see Supplementary Fig. S4). To reveal the effect of the SCO structure transition on the AHE, in Fig. 2d, we plot the anomalous Hall conductivity σ_{xy}^{AHE} (calculated by $\sigma_{xy}^{AHE} = \rho_{xy}^{AHE}/\rho_{xx}^2$) as a function of H at 2 K for the four SLs. Remarkably, the saturation value of σ_{xy}^{AHE} dramatically decreases with increasing n, from 0.34 S.cm^{-1} for C_6/S_1 SL to 0.006 S.cm^{-1} for C_6/S_4 SL. As reported, the intrinsic contribution of the AHE is the integral of the negative Berry

Fig. 3 Anisotropic magnetoresistance of CRO/SCO SLs. a Anisotropic magnetoresistance AMR for the C_6/S_1 SL on the LSAT substrate measured at temperatures ranging from 2 K to 100 K with the magnetic field rotated in the (100) plane. The inset plot shows the experimental setup. **b** Anisotropic magnetoresistance AMR for the C_6/S_n SLs on the LSAT substrates measured at 2 K with the magnetic field rotated in the (100) plane.

curvature over all occupied states in the entire Brillouin zone. In this case, ρ_{xy}^{AHE} follows the formula $\rho_{xy}^{AHE} = S_H \cdot \rho_{xx}^2(H, T) \cdot M(H, T)$, where the coefficient S_H is independent of H and T for each sample. In Fig. S4d, we plot ρ_{xy}^{AHE} (T) as a function of $\rho_{xx}^2(T)$ for the C_6/S_n SLs. Good linear scaling is observed for the C_6/S_1 and C_6/S_2 SLs in the temperature range below 20 K. This results indicate that the AHE is mainly determined by the intrinsic contribution and that σ_{xy}^{AHE} should follow the formula $\sigma_{xy}^{AHE} = S_H \cdot M(H, T)$, independent of the scattering rate. The sharp decrease in σ_{xy}^{AHE} indicates a decrease in magnetization or Berry curvature as n increases for C_6/S_n SLs. More importantly, the σ_{xy}^{AHE}-T curves in Fig. 2e provide information on the temperature dependence of magnetization for each SL. As demonstrated, the Curie temperature (T_C) is the highest (~75 K) for the C_6/S_1 SL. It decreases to ~30 K when $n = 2$ and to a value less than 5 K when n exceeds 3. Generally, the T_C of a ferromagnet is closely related to the strength of the FM exchange interaction. The highest T_C observed in the C_6/S_1 SL indicates that the emergent FM state tends to occur at the CRO/C-SCO interface. Along with the occurrence of the CRO/P-SCO interface, the interfacial FM order is strongly weakened and finally disappears, specifically, the FM exchange interaction in the interfacial CRO layers is efficiently controlled by the dimensionality of the nearby SCO layers.

Previous theoretical calculations predicted that a large tensile strain of 2 ~ 4% would result in an FM ground state for CRO films[32,33]. However, this topic remains debateable[34]. Structural analysis indicated that the C_6/S_n SLs were coherently strained to the LSAT substrate and suffered from a very low tensile strain (~0.4%). Thus, the emergent FM phase of the SLs is unlikely to be caused by the strain effect. To further confirm this inference, the transport properties are also measured for the C_6/S_n SLs on STO, which suffers from a relatively large tensile strain (~1.4%). The corresponding results are summarized in Fig. S5 in the Supplementary Materials. Hysteresis loops

of the ρ_{xy}^{AHE}-H curves are still observed for the C_6/S_1 and C_6/S_2 SLs on STO. However, based on the σ_{xy}^{AHE}-T curves, with the same n value, σ_{xy}^{AHE} and Tc of the SLs on STO are significantly lower than those of the SLs on LSAT. For example, the C_6/S_1 SL on STO has a Tc of 60 K and a maximal σ_{xy}^{AHE} of 0.05 S.cm^{-1}, while these are 75 K and 0.34 S.cm^{-1} for the C_6/S_1 SL on LSAT. Thus, the interfacial FM state is more robust in the SL on the LSAT substrate, although it suffers from a smaller tensile strain. A reasonable deduction is that the large tensile strain of the SLs on the STO substrate tends to induce a greater proportion of the CRO/P-SCO interface, which hinders the FM order[24].

The dimensional control of the interfacial FM phase is also reflected by the MR measurements. Figure 2f compares the out-of-plane (OP) *MR-H* curves at 2 K for the C_6/S_n SLs on LSAT. While the C_6/S_1 SLs show standard negative MR with butterfly shaped hysteresis, the other C_6/S_n SLs ($n \geq 2$) demonstrate a nonmonotonic MR dependence with evident positive contributions in the low-field region. This different MR dependence is similar to that for the SRO films subjected to different substrate strains; here, the negative MR was observed for the SRO films under compressive strain with a magnetic easy axis along the OP direction, and a nonmonotonic MR was observed for the SRO films under tensile strain with a magnetic easy axis deviating from the OP direction[35]. To determine the magnetic anisotropy, we further measured the anisotropic magnetoresistance (AMR) of the C_6/S_n SLs. The experimental setup is shown in the inset plot of Fig. 3a, where an electric current was applied along the [100] direction and the magnetic field of 9 T was rotated in the (100) plane perpendicular to the applied current. The AMR is defined by AMR $= (R_\theta - R_y)/R_y \times 100\%$, where R_y or R_θ is the resistance obtained with the magnetic field along the [010] direction or forming an angle of θ with the [010] direction, respectively. Figure 3a shows the AMR polar plots of C_6/S_1 SL measured at 2, 5, 10, 20, 50, and
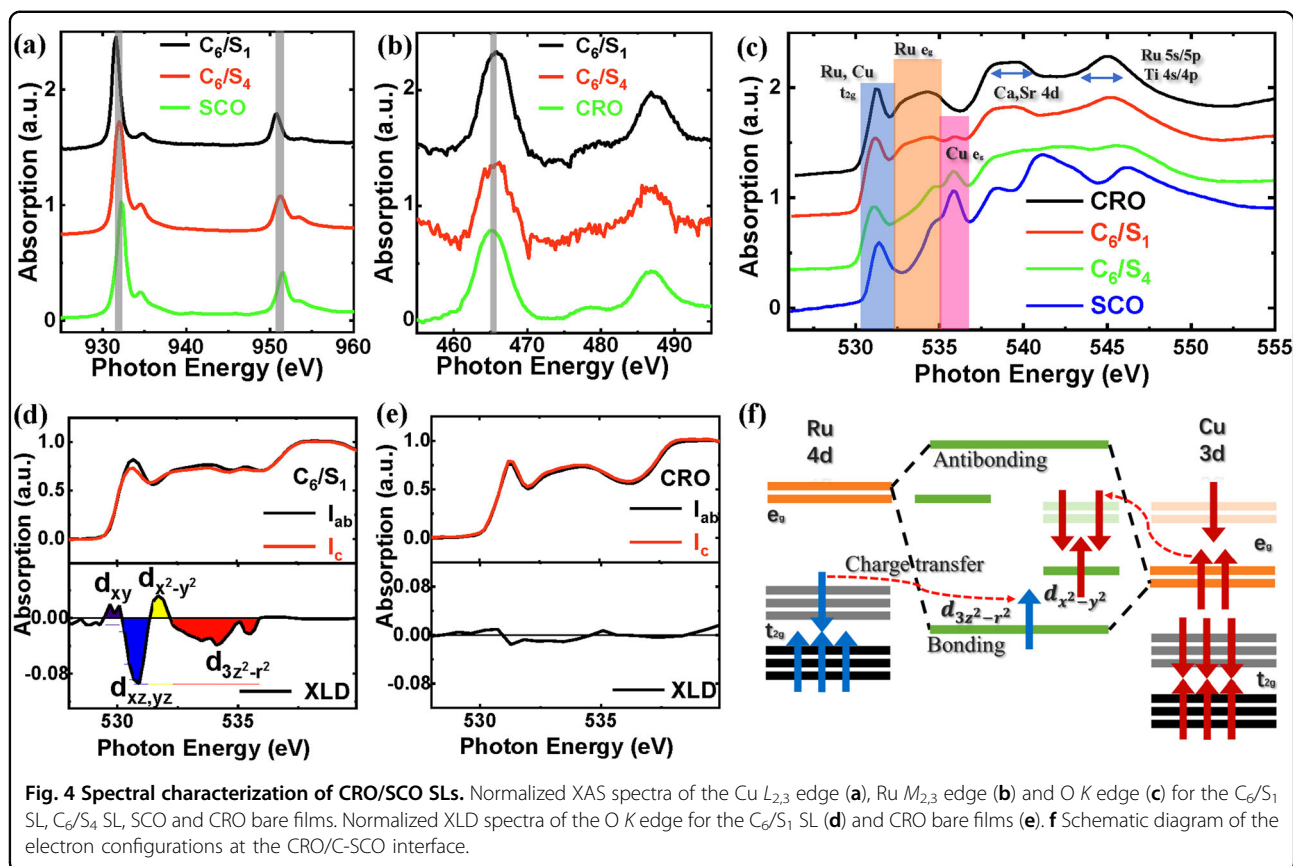
100 K. Although twofold symmetry is observed for all AMR curves, the two lobe peaks that correspond to the positions of the minimal resistance in the magnetic field have a 90° rotation across the T_c. At 2 K, the lobe peaks appear at $\theta = 90°$ (or 270°), with the largest amplitude of −0.18%. Then, the AMR amplitude gradually decreases with increasing temperature. Finally, when the temperature increases to 100 K, the peaks in the two lobes are horizontally arranged ($\theta = 0°$ or 180°). This result suggests that the magnetic easy axis of C_6/S_1 SL lies along the OP direction at low temperatures, where the minimal resistance appears due to the minimal spin-flip scattering when spins are fully aligned along the applied field. With increasing temperature, the magnetic field contribution decreases, and finally, other contributions from the normal AMR or Lorentz scattering become dominant, causing 90° rotation of the lobe peaks. Notably, the PMA is only observed in the C_6/S_1 SL, which has a robust FM order. As shown in Fig. 3b, the minimal resistances of the C_6/S_2, C_6/S_3 and C_6/S_4 SLs all occur at $\theta = 0°$ (or 180°) at 2 K. This is possibly because the contribution of spin-flip scattering cannot overcome the nonmagnetic contributions in these three SLs with relatively weak FM order.

Origin of interfacial ferromagnetism in CRO₆/SCOₙ superlattices

The above results indicate that the interfacial FM states in C_6/S_n SLs are strongly dependent on the structure of the SCO sublayers. To verify the difference in band structure between the CRO/C-SCO and CRO/P-SCO interfaces, we measured the soft XAS and XLD spectra around the Cu L-edge, Ru M-edge and O K-edge for the SLs as well as the bare films. We initially focused on the changes in the valence states of the Cu and Ru ions, determined by the XAS results with a 90° incident angle, as shown in Fig. 4a, b. Evidently, the Cu $L_{2,3}$-edges of the C_6/S_n SLs are shifted to lower energies than those of the SCO bare film. A significant left peak shift of ~0.6 eV is observed for C_6/S_1 SL, while it is only 0.2 eV for C_6/S_4 SL. Correspondingly, compared with the Ru^{4+} valence in the CRO bare film, the Ru $M_{2,3}$-edges show a higher energy shift of ~0.8 eV for C_6/S_1 SL and ~0.4 eV for C_6/S_4 SL. All these results consistently show that charge transfer from Ru^{4+} to Cu^{2+} occurs at the interface, resulting in $Ru^{4+\delta}$ and $Cu^{2-\delta}$ valence states. Generally, charge transfer between interfacial B-site ions are achieved via the O 2p orbital of apical oxygen ions. Thus, when the C-type SCO turns into P-type SCO at the interface, the interfacial charge transfer is significantly decreased due to the absence of apical oxygen ions. Moreover, the FM order is also weakened in the CRO/P-SCO interface as compared to the CRO/C-SCO interface, as mentioned above. Therefore, the Ru-to-Cu charge transfer is potentially responsible for the emergent FM state. Ordinary Hall curves confirmed the hole conduction type of the CRO sublayers in the SLs; this result was consistent with previous

reports[34]. Thus, electron transfer from Ru to Cu causes an increase in the hole density in the CRO sublayers. This result is directly evidenced by the measurements of the carrier densities, calculated by the slopes of the ordinary Hall terms. As shown in Fig. S6, the deduced n_h of the CRO sublayers at 50 K is 7.3×10^{20} cm^{-3} for C_6/S_4 SL, which gradually increases to 1.1×10^{21} cm^{-3} for C_6/S_3 SL, 2.1×10^{21} cm^{-3} for C_6/S_2 SL and 6.6×10^{21} cm^{-3} for C_6/S_1 SL. The 4d ruthenates CRO and SRO both have a narrow itinerant band composed of Ru t_{2g} and O 2p orbitals. FM exchange in SRO is generally understood based on the model of itinerant ferromagnetism, with a Stoner criterion of $IN(E_F)$ larger than 1; I is the Stoner parameter and $N(E_F)$ corresponds to the non-spin-polarized density of states (DOS) at the Fermi level. Bulk CRO has a small DOS at the Fermi level due to the large orthorhombic distortion of RuO_6, which results in an $IN(E_F)$ lower than 1 and, thus, a PM ground state. The accumulation of holes in the CRO layer sandwiched by C-SCO layers has possibly altered the Fermi-level DOS, resulting in an $IN(E_F)$ larger than 1. As a result, an FM ground state is achieved in the C_6/S_1 SL, similar to the exotic FM state in proton-intercalated $CaRuO_3$, as reported by ref. [36]. Apparently, due to the suppression of interface charge transfer, the T_c and magnetization decrease with increasing n.

In addition to changes in the valence state, charge transfer may also cause orbital reconstruction. As mentioned above, Ru-to-Cu charge transfer is mediated by the O $2p_z$ orbital of the apical oxygen ion. This causes an overlap of the $d_{3z^2-r^2}$ orbitals of the interfacial Ru and Cu ions, forming a Ru-O-Cu covalent bond at a low energy level. To experimentally evaluate this effect, we performed O K-edge XAS and XLD studies on the C_6/S_n SLs and the SCO and CRO bare films. Generally, the O K-edge peak stems from electron excitation from O 1s core level to unoccupied O 2p orbitals. The latter are strongly hybridized with the d orbitals of transition metal oxides near the Fermi level. In particular, the t_{2g} and e_g metal orbitals have π overlap and σ overlap with the O 2p states, respectively. Thus, the intensity of O K-edge peaks can reflect the number of empty d states. Furthermore, this has already been used to obtain information on the unoccupied states of Ru 4d orbitals[37–39]. As shown in Fig. 4c, five resonance features are identified around the O K-edge. According to the literature, the peak from 530.2 to 532.2 eV stems from hybridization with Ru t_{2g} orbitals, which partially overlaps with the Cu t_{2g} orbitals from 530.2 to 532.2 eV. The broad peak from 532.4 to 534.8 eV is related to hybridization with Ru e_g orbitals, and the relatively sharp peak from 534.8 to 537 eV is related to hybridization with Cu e_g orbitals. In the end, the structures from 537 to 549 eV are derived from the O 2p orbitals mixed into the (Sr,Ca) 4d, Ru 5s/5p and Cu 4s/4p states. Based on these analyses, we further measured the

Fig. 4 Spectral characterization of CRO/SCO SLs. Normalized XAS spectra of the Cu $L_{2,3}$ edge (**a**), Ru $M_{2,3}$ edge (**b**) and O K edge (**c**) for the C_6/S_1 SL, C_6/S_4 SL, SCO and CRO bare films. Normalized XLD spectra of the O K edge for the C_6/S_1 SL (**d**) and CRO bare films (**e**). **f** Schematic diagram of the electron configurations at the CRO/C-SCO interface.

O K-edge XLD spectra around the d orbital-derived region for the C_6/S_1 SL. The absorption signal I_{ab} obtained with X-ray polarization parallel to the [100] or [010] direction reflects the O $2p_x$ or $2p_y$ characteristics hybridized with the Ru d_{xy} and $d_{x^2-y^2}$ states. The I_c obtained with X-ray polarization nearly parallel to the [001] direction reflects the O $2p_z$ characteristic hybridized with the Ru d_{xz}, d_{yz} and $d_{3z^2-r^2}$ states. The negative XLD signals of ($I_c - I_{ab}$) around the e_g state and the t_{2g} state are observed for C_6/S_1 SL, while they are absent in the case of the CRO bare film (Fig. 4e). These results indicate that the e_g ($d_{3z^2-r^2}$ and $d_{x^2-y^2}$) and t_{2g} (d_{xz}, d_{yz} and d_{xy}) orbitals are degenerate by CRO/C-SCO interface coupling. Based on the above analysis of the XAS and XLD results, a schematic diagram of the electron configurations at the CRO/C-SCO interface is shown in Fig. 4f. The strong hybridization between the Ru and Cu $d_{3z^2-r^2}$ orbitals results in bonding (lower energy) and antibonding (higher energy) molecular orbitals at the interface; the former is lower than the upper t_{2g} orbital of Ru ions. Thus, the electrons in the upper t_{2g} orbital transfer to the Ru-O-Cu bonding orbital. On the one hand, this enhances the hole density in the CRO sublayers, inducing FM order. On the other hand, it causes the preferred occupancy of the $d_{3z^2-r^2}$ orbital, resulting

in perpendicular magnetic anisotropy in C_6/S_1 SL according to the Bruno model. All these observations indicate that dimensional control of the interfacial FM state in C_6/S_n SL is predominantly achieved by modulating the interfacial charge transfer.

Conclusion

In summary, we successfully induced FM order into the original PM CRO layers by the proximity of the C-type SCO layers. The emergent interfacial FM phase processes with the highest Tc of ~75 K and perpendicular magnetic anisotropy were confirmed by Hall and magnetoresistance measurements. The XAS spectra reveal significant charge transfer from Ru-to-Cu sites at the CRO/C-SCO interface, which results in an increase in the hole density and, thus, FM order in the CRO interfacial layers. This also causes the reconstruction of Ru 4d bands, leading to $d_{3z^2-r^2}$ orbital polarization. Dimensional control of the interfacial FM phase is further achieved by modulating the strength of the charge transfer at the CRO/SCO interface. We anticipate that these results can facilitate the dimensional control of interface coupling and thus form emergent interfacial phases at perovskite/infinite-layered oxide heterostructures, establishing a novel platform for exotic quantum phenomena.

Materials and methods

Thin-film growth

High-quality CRO/SCO SLs were epitaxially grown on (001)-oriented LSAT and STO substrates by pulsed laser deposition (KrF, $\lambda = 248$ nm). CRO and SCO bare films were also prepared for comparison. The sample growth was conducted at 670 °C with an oxygen pressure of 30 Pa and a laser fluence of 2.5 J/cm^2. After deposition, the sample was cooled to room temperature in the furnace with an oxygen pressure of 100 Pa. The deposition rates for the CRO layer and SCO layer were carefully calibrated via the technique of small-angle X-ray reflectivity (XRR; see Fig. S1b).

Sample characterization

The surface morphology of the as-prepared films was evaluated via atomic force microscopy (AFM, SPI 3800 N, Seiko). The crystal structure was determined by high-resolution X-ray diffractometry (XRD, D8 Discover, Bruker) with Cu-Kα radiation. Transport measurements were performed via Quantum Designed physical property measurement system (PPMS) using a Hall bar geometry with a width of 200 μm and a length of 1300 μm. The measurements were performed in DC mode, with an applied current of 100 μA.

X-ray absorption spectroscopy

XAS measurements were performed at the BL08U1A beamline in the Shanghai Synchrotron Radiation Facility at room temperature in total electron yield mode. The XLD spectra of the oxygen K edge and the cuprate L edge were measured for the two polarization directions of the linearly polarized X-ray with an incident angle of 70° to the film normal. *E* is the electric field of the X-ray. I_{ab} (*E*//[100] or [010]) and I_c (*E*//[001]) are the absorption intensities corresponding to the IP direction and the OP direction, respectively. The measurement temperature was 300 K.

Author details
^{1}Beijing National Laboratory for Condensed Matter Physics and Institute of Physics, Chinese Academy of Sciences, Beijing 100190, China. ^{2}School of Physical Sciences, University of Chinese Academy of Sciences, Beijing 100049, China. ^{3}School of Integrated Circuit Science and Engineering, Beihang University, Beijing 100191, China. ^{4}CAS Key Laboratory of Standardization and Measurement for Nanotechnology, National Center for Nanoscience and Technology, Beijing 100190, China. ^{5}Ningbo Institute of Materials Technology & Engineering, Chinese Academy of Sciences, Ningbo, Zhejiang 315201, China. ^{6}Spintronics Institute, School of Physics and Technology, University of Jinan, Jinan 250022, China

Conflict of interest
The authors declare no competing interests.

Publisher's note
Springer Nature remains neutral with regard to jurisdictional claims in published maps and institutional affiliations.

References
1. Li, D. et al. Superconductivity in an infinite-layer nickelate. *Nature* **572**, 624 (2019).
2. Imada, M., Fujimori, A. & Tokura, Y. Metal-insulator transitions. *Rev. Mod. Phys.* **70**, 1039 (1998).
3. Wang, J. et al. Epitaxial BiFeO$_3$ multiferroic thin film heterostructures. *Science* **299**, 1719 (2003).
4. Wang, K. F., Liu, J. M. & Ren, Z. F. Multiferroicity: the coupling between magnetic and polarization orders. *Adv. Phys.* **58**, 321 (2009).
5. Umezawa, A. et al. Flux pinning, granularity and the irreversibility line of the high-T$_c$ superconductor HgBa$_2$Cu0$_{4+}$ x. *Nature* **364**, 129 (1993).
6. Park, J.-H. et al. Direct evidence for a half-metallic ferromagnet. *Nature* **392**, 794 (1998).
7. Lodahl, P. et al. Controlling the dynamics of spontaneous emission from quantum dots by photonic crystals. *Nature* **430**, 654 (2004).
8. Ohtomo, A., Muller, D. A., Grazul, J. L. & Hwang, H. Y. Artificial charge-modulationin atomic-scale perovskite titanate superlattices. *Nature* **419**, 378 (2002).
9. Song, C., Havlin, S. & Makse, H. A. Self-similarity of complex networks. *Nature* **433**, 392 (2005).
10. Yadav, A. K. et al. Observation of polar vortices in oxide superlattices. *Nature* **530**, 198 (2016).
11. Trier, F. et al. Quantization of hall resistance at the metallic interface between an oxide insulator and SrTiO$_3$. *Phys. Rev. Lett.* **117**, 096804 (2016).
12. Okamoto, S. & Millis, A. J. Electronic reconstruction at an interface between a Mott insulator and a band insulator. *Nature* **428**, 630 (2004).
13. Mannhart, J. & Schlom, D. G. Oxide interfaces—an opportunity for electronics. *Science* **327**, 1607 (2010).
14. Liu, X. et al. Magnetoelectric phase transition driven by interfacial-engineered Dzyaloshinskii-Moriya interaction. *Nat. Commun.* **12**, 5453 (2021).
15. Matsuno, J. et al. Interface-driven topological Hall effect in SrRuO$_3$-SrIrO$_3$ bilayer. *Sci. Adv.* **2**, e1600304 (2016).
16. Caputo, M. et al. Proximity-induced novel ferromagnetism accompanied with resolute metallicity in NdNiO$_3$ heterostructure. *Adv. Sci. (Weinh.)* **8**, e2101516 (2021).
17. Yoo, M.-W. et al. Large intrinsic anomalous Hall effect in SrIrO$_3$ induced by magnetic proximity effect. *Nat. Commun.* **12**, 3283 (2021).

18. Klein, L., Antognazza, L., Geballe, T. H., Beasley, M. R. & Kapitulnik, A. Possible non-Fermi-liquid behavior of $CaRuO_3$. *Phys. Rev. B* **60**, 1448 (1999).

19. Mazin, I. I. & Singh, D. J. Electronic structure and magnetism in Ru-based perovskites. *Phys. Rev. B* **56**, 2556 (1997).

20. Dang, H. T., Mravlje, J., Georges, A. & Millis, A. J. Electronic correlations, magnetism, and Hund's rule coupling in the ruthenium perovskites $SrRuO_3$ and $CaRuO_3$. *Phys. Rev. B* **91**, 195149 (2015).

21. Jakobi, E., Kanungo, S., Sarkar, S., Schmitt, S. & Saha-Dasgupta, T. LDA +DMFTstudy of Ru-based perovskite $SrRuO_3$ and $CaRuO_3$. *Phys. Rev. B* **83**, 041103 (2011).

22. Kennedy, R. J., Madden, R. & Stampe, P. A. Effects of substrate temperature on the growth and properties of $SrRuO_3$ and $CaRuO_3$ thin films. *J. Phys. D Appl. Phys.* **34**, 1853 (2001).

23. Samal, D. et al. Experimental evidence for oxygen sublattice control in polar infinite layer $SrCuO_2$. *Phys. Rev. Lett.* **111**, 096102 (2013).

24. Zhong, Z., Koster, G. & Kelly, P. J. Prediction of thickness limits of ideal polar ultrathin films. *Phys. Rev. B* **85**, 121411 (2012).

25. Liao, Z. et al. Large orbital polarization in nickelate-cuprate heterostructures by dimensional control of oxygen coordination. *Nat. Commun.* **10**, 589 (2019).

26. Li, S. et al. Strong ferromagnetism achieved via breathing lattices in atomically thin cobaltites. *Adv. Mater.* **33**, e2001324 (2021).

27. Zhou, G. et al. Dimensionality control of magnetic coupling at interfaces of cuprate-manganite superlattices. *Mater. Horiz.* **8**, 2485 (2021).

28. Li, Z. et al. Infinite-layer/perovskite oxide heterostructure-induced high-spin states in $SrCuO_2/SrRuO_3$ bilayer films. *Mater. Horiz.* **8**, 3468 (2021).

29. Lin, S. et al. Dimensional control of octahedral tilt in $SrRuO_3$ via infinite-layered oxides. *Nano Lett.* **21**, 3146 (2021).

30. Taguchi, Y., Matsumoto, T. & Tokura, Y. Dielectric breakdown of one-dimensional Mott insulators Sr_2CuO_3 and $SrCuO_2$. *Phys. Rev. B* **62**, 7015 (2000).

31. Jaiswal, A. K. et al. Direct observation of strong anomalous Hall effect and proximity-induced ferromagnetic state in $SrIrO_3$. *Adv. Mater.* **34**, e2109163 (2022).

32. Zayak, A. T., Huang, X., Neaton, J. B. & Rabe, K. M. Manipulating magnetic properties of $SrRuO_3$ and $CaRuO_3$ with epitaxial and uniaxial strains. *Phys. Rev. B* **77**, 214410 (2008).

33. Zhang, J. et al. Density functional theory-based prediction of the pressure-dependent magnetic properties of $CaRuO_3$. *Phys. Status Solidi (b)* **259**, 2100290 (2021).

34. Tripathi, S. et al. Ferromagnetic $CaRuO_3$. *Sci. Rep.* **4**, 3877 (2014).

35. Tian, D. et al. Manipulating Berry curvature of $SrRuO_3$ thin films via epitaxial strain. *Proc. Natl Acad. Sci. USA* **118**, e2101946118 (2021).

36. Shen, S. et al. Emergent ferromagnetism with fermi-liquid behavior in proton intercalated $CaRuO_3$. *Phys. Rev. X* **11**, 021018 (2021).

37. Schmidt, M. et al. Nature of the electronic states in the layered perovskite noncuprate superconductor Sr_2RuO_4. *Phys. Rev. B* **53**, R14761 (1996).

38. Mizokawa, T. et al. Spin-orbit coupling in the Mott insulator Ca 2 RuO 4. *Phys. Rev. Lett.* **87**, 077202 (2001).

39. Malvestuto, M. et al. Electronic structure trends in the $Sr_{n+1}Ru_nO_{3n+1}$ family ($n= 1, 2, 3$). *Phys. Rev. B* **83**, 165121 (2011).